Nanoscale

ARTICLE

Electronic Supplementary Material

Ultrasensitive, flexible, and low-cost nanoporous piezoresistive composite for tactile pressure sensing

Jing Li,[a,b,c,†] Santiago Orrego,[a,b] Junjie Pan,[a,b] Peisheng He[a,b] and Sung Hoon Kang*[a,b]

[a] Department of Mechanical Engineering, Johns Hopkins University, Baltimore, MD 21218, USA. E-mail: shkang@jhu.edu
[b] Department of Mechanical Engineering, Johns Hopkins University, Baltimore, MD 21218, USA
[c] Hubei Key Laboratory of Advanced Technology for Automotive Components, Wuhan University of Technology, Wuhan, Hubei, 430070, China
[†] Present address: School of Mechanical Engineering, Hubei University of Technology, Wuhan, Hubei, 430068, China

Contents

1. Details of the nanoporous polymer composite (NPC) fabrication processes and scanning electron microscopy (SEM) images of the composites before and after acid etching

2. The equivalent circuit of resistance measurements

3. The schematic model of the three-regime piezoresistive response of the NPC

4. The comparison of sensing performance and cost of our sensor with those of the pressure sensors from previous works

5. The repeatability of the NPC sensor signals under periodic dynamic loadings

6. Piezoresistive response of the NPC sensor to water droplets

7. Piezoresistive response of the NPC sensor to footsteps of a cockroach

8. Piezoresistive response of the NPC sensor to cyclic finger tapping

9. Piezoresistive response of the NPC sensor to weight loading

1. Details of the nanoporous polymer composite (NPC) fabrication processes and scanning electron microscopy (SEM) images of the composites before and after acid etching

(1) The fabrication process of the NPC is as follows (Fig. S1):

STEP 1: ZnO NPs were first dispersed in PDMS (Sylgard 184, Dow Corning) monomer using revolutionary mixer (KK-400W, Mazerustar) for 360 seconds (channel 10: 7 revolutions, 3 rotations in 90 seconds). The mass ratio between ZnO NP to PDMS was adjusted to create different porosities. At this step, we can get ZnO NP/PDMS monomer mixture.

STEP 2: The PDMS curing agent was added to the mixture from STEP 1, which was then uniformly dispersed using revolutionary mixer for 90 seconds. The mass ratio between the PDMS monomer and curing agent was 10:1. Subsequently, 15 wt % MWCNTs (US Research Nanomaterials, Inc) were mixed with the mixture using revolutionary mixer for 270 seconds. Then, highly viscous MWCNT/ZnO NP/PDMS mixture was obtained.

STEP 3: The mixture was then cured in an oven (Lindberg Blue M from Thermo Fisher Scientific) at 60 °C for 6 hours. Subsequently, the solidified composite was placed at room temperature for 24 hours to ensure that the MWCNT/ZnO NP/PDMS mixture was completely cured. The mixture was then immersed in hydrochloric acid solution (ACS reagent 37%, Sigma-Aldrich) for 4 hours to completely remove the ZnO NPs. Then, the material was washed with deionized (DI) water and piezoresistive nanoporous polymer composite was obtained. The synthesized NPC could be cut into different shapes and/or sizes according to experimental requirements.
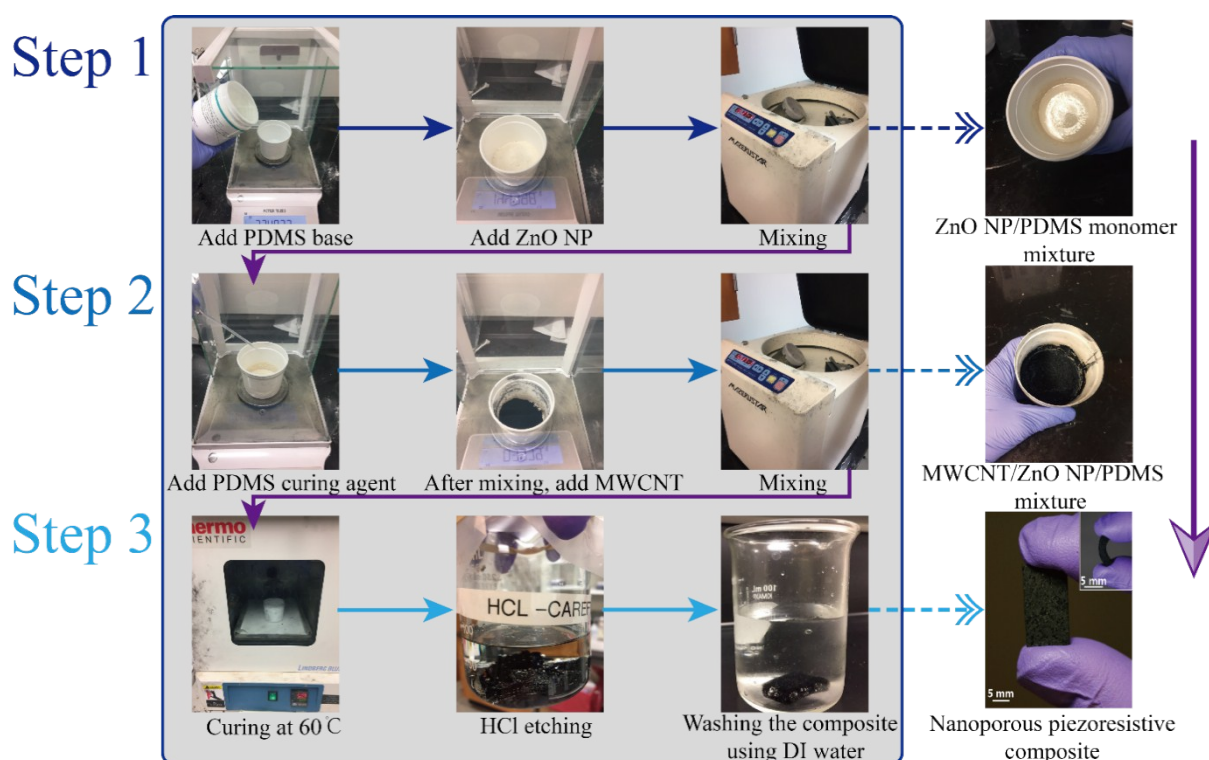
**Figure S1.** Schematic diagrams of the NPC synthesis process.

(2) Conductive electrodes for the as-fabricated nanoporous piezoresistive composite

To have reliable bonding condition of the copper tape, before we put the copper tape to the sample, we first polished the sample surface using sand paper and we used the ultrasonication bath to remove the dust and did plasma-treatment to improve the adhesion of the NPC. Then, we put the copper tape to the surface of the sample and put weight on top of it

overnight. And, to make sure there is reliable electrical connection, we first measured the resistivity of the NPC using digital source meter (Keithley 2400). We measured the resistance of the NPC sample with copper tape and known geometry. Based on the relation between resistivity and resistance ($\rho = RA/L$, ρ: resistivity, R: resistance, A: area, L: thickness), we calculated the resistivity and compared with the measured data in Figure 2c (manuscript) to make sure the electrical connection is reliable. Additionally, to minimize the influences of electrode, during the quantification of the piezoresistive performance of the NPCs, the sample was sandwiched between two electrodes comprised of copper tapes bonded to the loading fixtures and connected to the DAQ (see Supporting Information 2 for details). Furthermore, we have done many cyclic loading tests such as Figures 3c&d and Figures 4e&f (manuscript) and found the resistance changes were very reproduceable. So, we think the response on force application is due to the composite.

(3) SEM images of the composites before and after HCl acid etching

To check the formation of porous structures by etching of sacrificial ZnO nanoparticles, we used SEM as described below. The NPCs were fabricated by adding sacrificial ZnO nanoparticles (ZnO NPs) (US Research Nanomaterials, Inc) to multi-wall carbon nanotube (MWCNT) /polydimethylsiloxane (PDMS) mixture, followed by hydrochloric acid (HCl, ACS reagent 37%, Sigma-Aldrich) etching. To check the effect of etching, SEM images were taken by Tescan Mira 3 GM scanning electron microscope before and after etching (Fig. S2). Before acid etching (Fig. S2, left), the surface of the ZnO/MWCNT/PDMS composite was very rough and there were lots of visible particles. It was considered that the surface of the ZnO/MWCNT/PDMS composite was covered by ZnO NPs before acid etching. After etching the ZnO NPs, a porous structure was created. We can see the PDMS matrix was embedded with MWCNTs only (tube-like objects in Fig. S2, right) and the part of the MWCNTs were exposed.
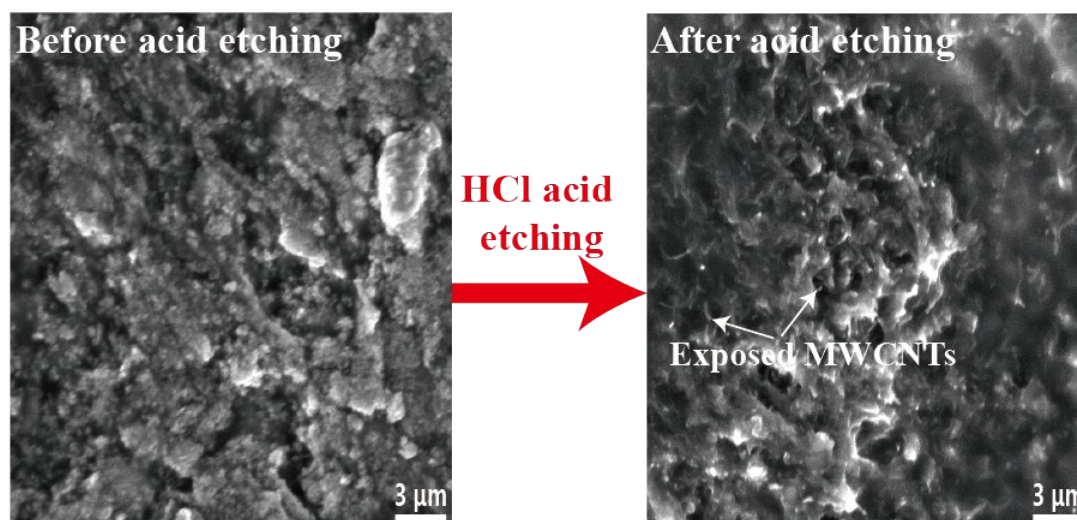

Figure S2. Scanning electron microscopy (SEM) images the composites before and after acid etching.

2. The equivalent circuit of resistance measurements

To quantify the piezoresistive performance of the NPCs, we used a combination of an electromechanical testing frame (MTS Insight 5, Eden Prairie, MN) to deform the samples and a data acquisition system (DAQ, National Instruments USB 6210) to measure changes in resistance upon loading. The NPC was subjected to compression load at a strain rate of 4×10^{-4} s^{-1} by utilizing a load cell (LSB-200, Futek) of 10 N capacity. The sample was sandwiched between two electrodes comprised of copper tapes bonded to the loading fixtures and connected to the DAQ. The electric signals from the NPC and the testing frame were acquired by the DAQ and then transferred to a personal computer (PC) for recording using LabView (Fig. S3a). To calculate the resistance changes on the NPC, we used an equivalent circuit with a shunt resistor (R) in series with known value (10 MΩ) as shown in Fig. S3b. The applied voltage ($V_{DD\text{-}GND}$) across the circuit was set at 5 V. The shunt ($V_{DD\text{-}GND}$-$V_{x\text{-}GND}$) and the NPC ($V_{x\text{-}GND}$) voltages were measured by the DAQ. Since the circuit is in series, the current through each of the components is the same, and the voltage across the circuit is the sum of the voltages. Therefore, the resistance of the NPC (R_x) can be calculated as

$$R_x = \frac{V_{x-GND}}{V_{DD-GND} - V_{x-GND}} \times R$$

(S1)
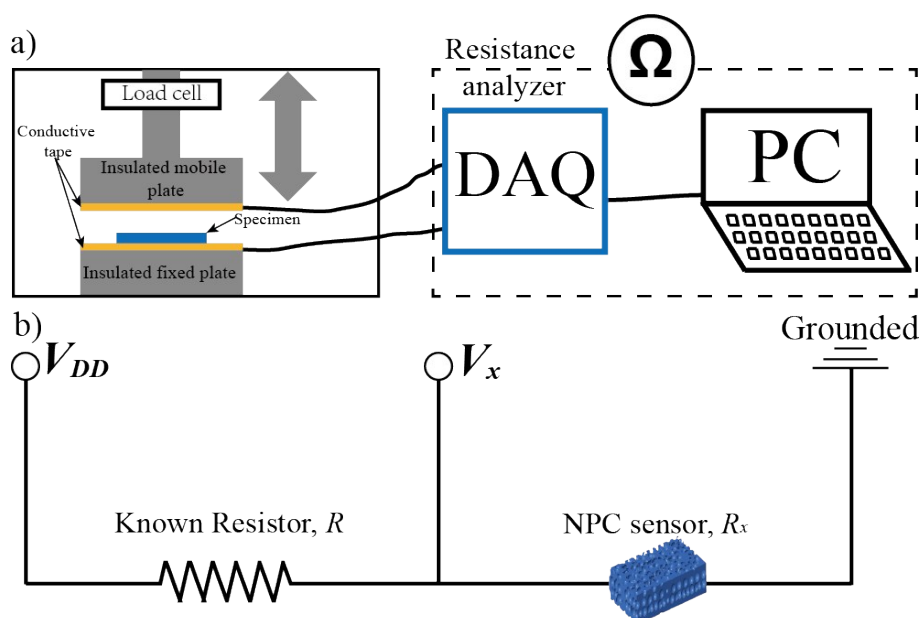
Figure S3. a) Schematic of the electro-mechanical characteristic measurement set-up to measure the piezoresistive response of the NPC and b) the equivalent circuit of resistance measurements.

3. The schematic model of the three-regime piezoresistive response of the NPC

The three-regime piezoresistive response of the NPC could be attributed to the progressive formation of conductive pathways upon loading at different strain levels as shown in Fig. S4. In the schematic, we assume the pores are uniformly distributed and the pore is spherical with a constant radius (r) (see Fig. S4, left). Before loading, in stage I, the exposed MWCNTs within the pores are expected to have low connections. After initiating compressive loading, nanoscale pores would begin to collapse connecting the exposed MWCNTs at the internal pore surfaces. And, it is known that the piezoresistive sensitivity (strain gauge factor, GF) is related to the fractional resistance change ($\Delta R/R_0$) and the action strain (ε) as $GF = (\Delta R/R_0)/\varepsilon$.[1] The action strain is related to the action distance (l) between the top and the bottom sides MWCNTs networks, as $\varepsilon = l/L$ (where L is the length of the NPC along the loading direction). As the action distance is proportional to pore size (r), the significantly decreased pore size will lead to extremely shortened action distance (or strain ε), resulting higher resistance change with strain. Hence, the small pore diameter (~50 nm) of the NPC would contribute to ultra-sensitivity of sensor at lower strains. Therefore, within regime I, there would be a sharp resistivity drop and the resulting rapid increase of the fractional resistance change ($\Delta R/R_0$).
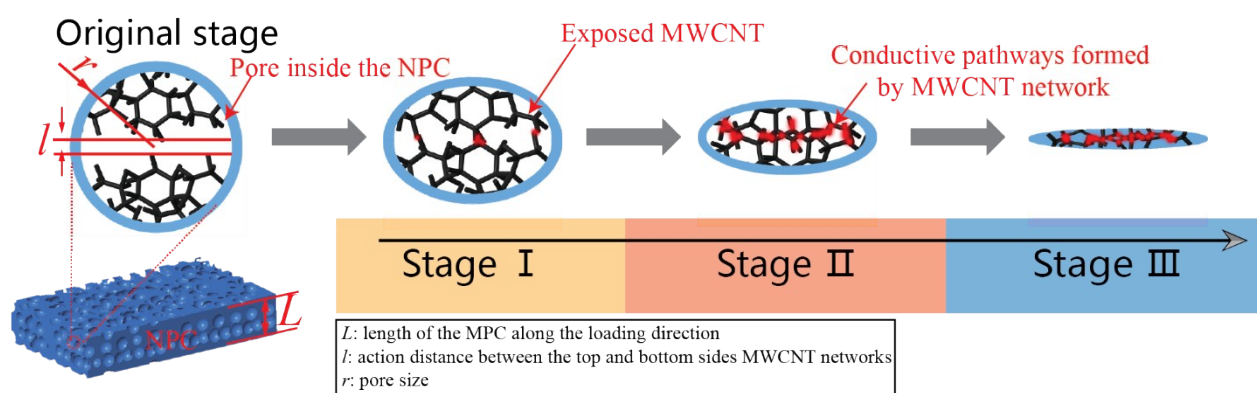
Figure S4. Schematic of the three-regime sensitivity responses of the NPC from the progressive formation of conductive pathways upon loading.

As the compressive loading continues (stage II), additional conductive paths (marked by red color in Fig. S4) are established. The change of the contact area among the conductive materials with the compressive loading determines the piezoresistive sensing performance.[2] And, the piezoresistive sensitivity is proportional to the change of the conductive pathways formed by the interaction of the exposed conductive MWCNT networks. For a porous specimen with a given geometry, the interaction area would be related to the pore surface area (S_{pore}), which is related to the pore number (n) and pore size (r). From our assumptions that the pores are uniformly distributed and the pore shape is spherical with a constant radius (r), the total pore surface area (S_{pore}) can be described as

$$S_{pore} = 4\pi r^2 n = \frac{3PV}{r} \qquad (S2)$$

where V is the volume of the porous material and n is determined by the porosity (P) and pore size (r), as $n = VP/v = 3VP/4\pi r^3$, where v is the pore volume. Thus, the pore surface area (S_{pore}) is proportional to the porosity and inversely proportional to the pore size. As the piezoresistive sensitivity is directly related to the pore surface area, the piezoresistive sensitivity can be improved by the decreasing pore size and increasing porosity. Thus, besides increasing the porosity, which is demonstrated in Fig. 2d, we can have the higher sensitivity as we decrease the pore size from micro to nano, due to the increased contact surface area. Therefore, in stage II, the increased conductive paths could be established by the continuous collapsing/closure of pores as the strain increases, which further reduces resistance.

Once the pores are fully closed in stage III (Fig. S4, right region), the sensitivity of NPC would reduce and the bulk effect becomes dominant. The conductive pathways increase due to the viscous properties of the PDMS matrix making the MWCNTs mobile.[3]

4. The comparison of sensing performance and cost of our sensor with those of the pressure sensors from previous works

Firstly, we summarized the recent progress of the most frequently used electromechanical (piezoelectric, capacitive and piezoresistive) pressure sensors. As shown in Table S1, the basic sensing performance such as pressure sensitivity, detection limit, and response time were compared. From the comparison, piezoresistive materials generally have higher pressure sensitivity and lower detection limit than most of piezoelectric and capacitive sensors. To be noticed, our work showed a higher sensitivity and faster response time among piezoresistive sensors.

Table S1. Comparison of electromechanical sensors and their performance parameters.

Sensing mechanism	Materials	Pressure sensitivity	Detection limit	Response time	Ref.
Piezoelectricity	PVDF	2 kPa^{-1}	1 kPa		4
Piezoelectricity	P(VDF-TrFE)		200 kPa		5
Piezoelectricity	P(VDF-TrFE)	1.1 kPa^{-1}	0.1 Pa		6
Piezoelectricity	P(VDF-TrFE)	2.3 kPa^{-1}		170 ms	7
Piezoelectricity	P(VDF-TrFE)		13.3 Pa		8
Piezoelectricity	ZnO	2.1 kPa^{-1}	3.5 kPa	150 ms	9
Piezoelectricity	Polypropylene	1×10^{-3} kPa^{-1}	2 Pa		10
Piezoelectricity	Titanate/P(VDF-TrFE)	6.7×10^{-4} kPa^{-1}	200 kPa		11
Optical waveguide	PDMS	0.2 kPa^{-1}	<1 kPa	300 ms	12
Capacitance	GaN	8.6×10^{-3} kPa^{-1}			13
Capacitance	Fluorosilicone	0.91 kPa^{-1}			14
Capacitance/OFET	PS-*b*-P2VP	1.76 kPa^{-1}	<17 kPa		15
Capacitance/OFET	PDMS/Rubrene	0.55 kPa^{-1}	3 Pa	<10 ms	16
Capacitance/OFET	PDMS/Pil2TSi	8.4 kPa^{-1}		<10 ms	17
Piezoresistivity	**PDMS/MWCNTs**	**13.3 kPa^{-1}**	**<2 Pa**	**<70 ms**	**Our work**
Piezoresistivity	PDMS/SWNTs	0.23 kPa^{-1}	50 kPa	≤125 ms	18
Piezoresistivity	PDMS/SWNTs	1.8 kPa^{-1}	0.6 Pa		19
Piezoresistivity	Double-layered graphene	0.24 kPa^{-1}	0.3 Pa		20
Piezoresistivity	Graphene-polyurethane sponge	0.26 kPa^{-1}	9 Pa		21

In Table S2, we compared the performance/price ratio of our NPC sensor with other reported piezoresistive sensors. The performance/price ratio was calculated from the unit price of the active materials and the strain gauge factor. For the price calculation, we just considered the active materials cost and the matrix cost by checking the unit price for each active material obtained from vendors such as US Research Nanomaterials, Inc. and Sigma-Aldrich. Then, based on the composition mentioned in the reference papers, we calculated the total material price using the following equation: $P = P_0 * \eta_0 + P_1 * \eta_1$, where P is the price of the composite; P_0 and P_1 are the unit prices of the active material and the matrix material, respectively; η_0 and η_1 are the fractions of the active material and the matrix material. The marked symbol (*) indicates the requirement of special technique/equipment during the fabrication process, such as chemical vapor deposition or ultraviolet exposure. The sensing performance-to-price ratio (gauge factor/material cost) of our work (NPC with ~15.8% porosity) is >226 which is at least an order of magnitude higher than those of previous studies, to the best of our knowledge.

Table S2. Comparison of the sensing performance and material cost of the piezoresistive pressure sensors from reported works. The marked symbol (*) indicates the requirement of special technique/equipment during the fabrication process.

Materials	Strain gauge factor (GF)	Unit price of the active materials ($/g)	Performance-price ratio	Ref.
PDMS/MWCNT	**306**	**1.35**	**226.67**	**Our work**
PDMS/MWCNT/CB*	29.1	1.2	24.25	22
PDMS/MWCNT	11	1.35	8.15	23
PDMS/MWCNT sponge	2	1.35	1.48	24
Sponge/MWCNT/Ag NP	6.13	25	0.25	25
PU/MWCNT	3	1.35	2.22	26
PMMA/SWMT	5.2	140	0.04	27
Fragmentized graphene foam*	29	195	0.15	28
PVDF/graphene	12	195	0.06	29
Putty/graphene	450	195	2.31	30
3D graphite*	50	8	6.25	31
Interlocked PUA*	11.45	14.9	0.77	32
PDMS/Ag nanowire*	14	100	0.14	33

### 5. The repeatability of the NPC sensor signals under periodic dynamic loadings

We investigated the repeatability of the sensing signals by conducting tests under periodic dynamic loadings. As the schematic in Fig. S5, cyclic loading was applied using a long-stroke shaker (113 Electro-Seis®, APS Dynamics Inc.) and the electric signals were acquired by DAQ. The shaker setup consists of a load cell (LSB-200, 10 N, Futek) and a displacement sensor to calculate stress-strain relationships. All the measurement data from the DAQ were recorded by a personal computer.
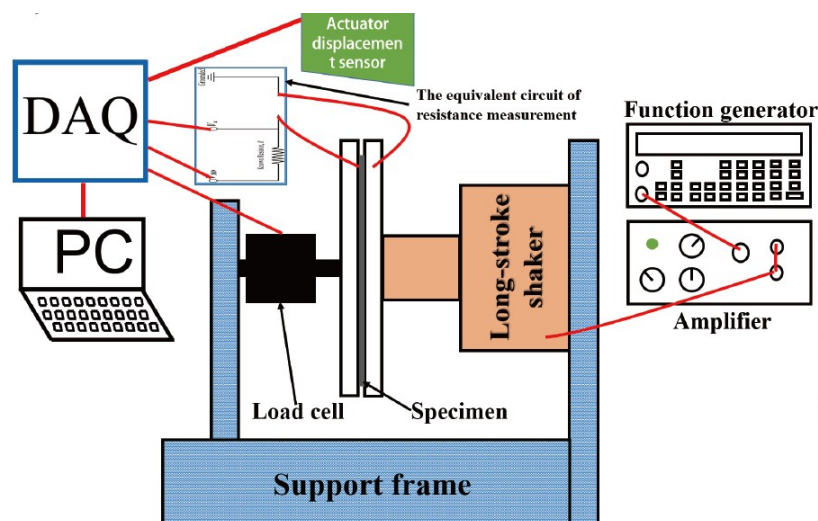
Figure S5. Schematic of the dynamic loading measurement set-up.

6. Piezoresistive response of the NPC sensor to water droplets

To demonstrate the applications of the NPC for sensing subtle pressure, a rectangular NPC with an area of 2 cm^2 was sandwiched by conductive copper tapes as a pressure sensor. The conductive tapes were connected to a digital source meter (Keithley 2400) to detect the resistance signals. Simultaneously, the sensing process was recorded using a digital camera (EOS 70D, Canon). The real-time fractional resistive response is plotted in Fig. S6 as water droplets (30-50 mg per water droplet, inset in Fig. S6) were placed on the NPC pressure sensor using a pipet (available from VWR). The insets are the images recorded by the digital camera, showing the resistance change during the measurement process.
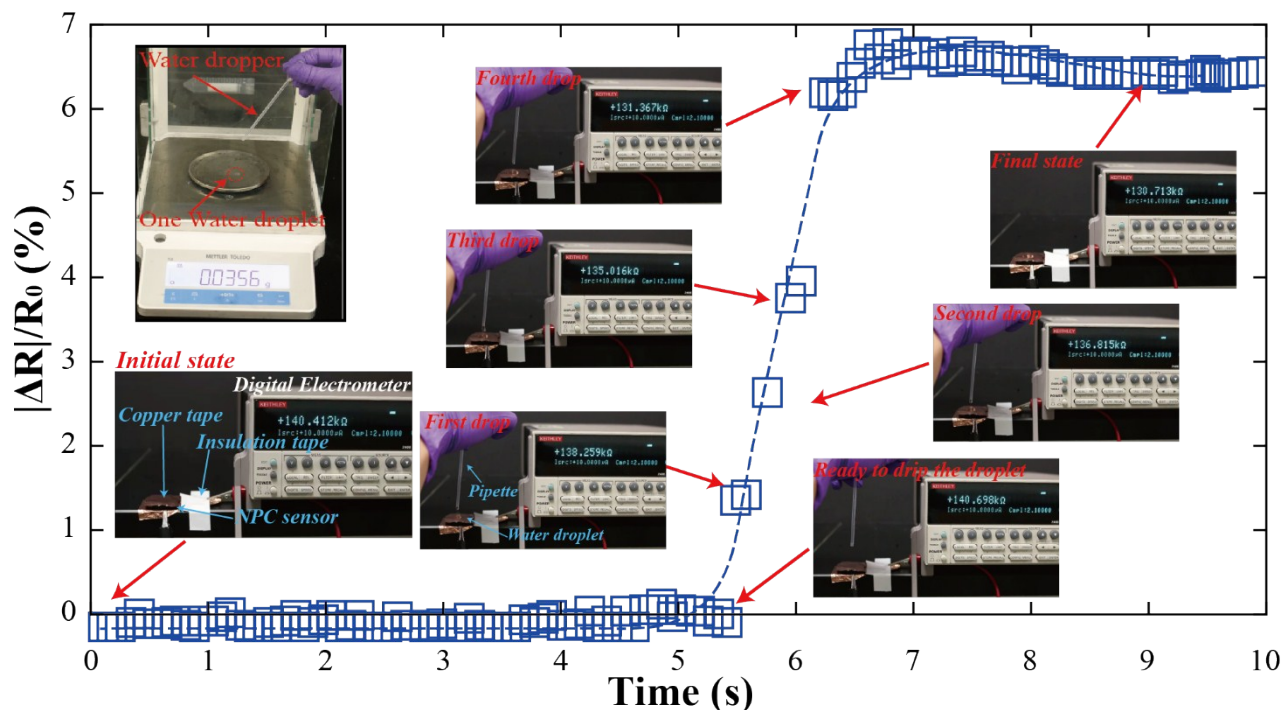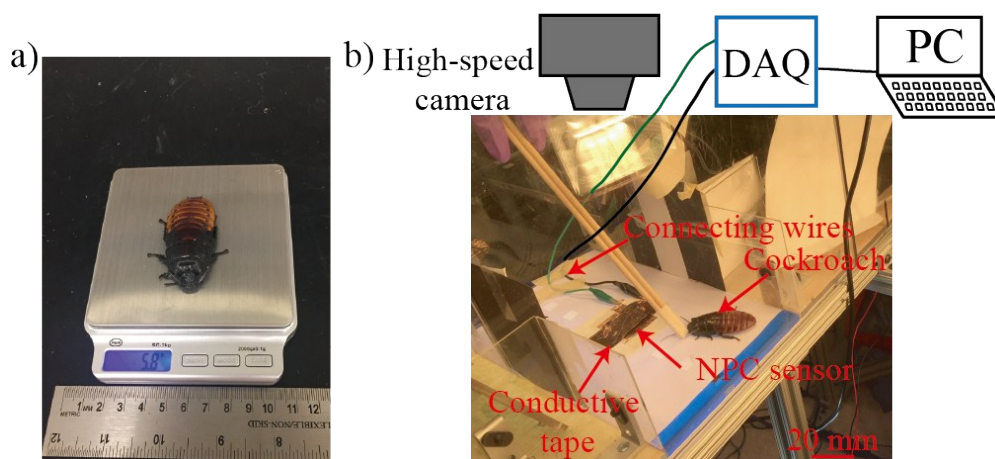

Figure S6. The real-time fractional resistance changes to water droplet loading (the insets are the images recorded by the digital camera, showing the actual resistance change during the measurement process and the measured weight of one droplet water using an analytical balance.

7. Piezoresistive response of the NPC sensor to footsteps of a cockroach

(1) Details of the cockroach and the sensing measurement set-up

We tested our NPC sensor for detecting movement of a cockroach. Fig. S7a shows the image of the cockroach used in the experiment. The weight of the cockroach was 5.8 gram. Fig. S7b shows the set-up for measuring cockroach walking. The cockroach was put in a transparent box, while the NPC pressure sensor with an area of 2 cm² was fixed to the bottom surface of box. Simultaneously, the walking of the cockroach was recorded by the Bitflow high-speed camera (100 frames/s), fixed above the box.


Figure S7. a) The image of the cockroach used in the experiment. b) The set-up for measuring cockroach walking.

(2) Details of the cockroach walking measurements

The real-time fractional resistance changes are plotted in Fig. S8a and the Fig. S8b shows the corresponding images captured by the high-speed camera. Numbers in Fig. S8a show the data points in the different states of the cockroach movement and the images in Fig. S8b are the corresponding pictures to the resistance signals in Fig. S8a. In the images of Fig. S8b, the highly-reflective metal films appear to be highly wrinkled due to the spotlights for high-speed imaging. The state of the cockroach during its walking period was as follows:

1: The cockroach is far away from the NPC sensor, 2: The cockroach approaches the NPC sensor, 3: The first footstep of the cockroach passed through the sensor, 4: The second footstep was placed on the sensor, 5: The third footstep was placed, 6: The forth footstep was placed, 7: The fifth footstep was placed, 8: The cockroach passed the sensor. By comparing the time stamp of the high-speed video with the resistance signals, we found that the five peak electric signals (Fig. S8a) were generated with the five footsteps (one footstep is one cycle of lifting up the leg and putting it down) of the cockroach, demonstrating both high sensitivity and fast electrical response of our NPC pressure sensor.
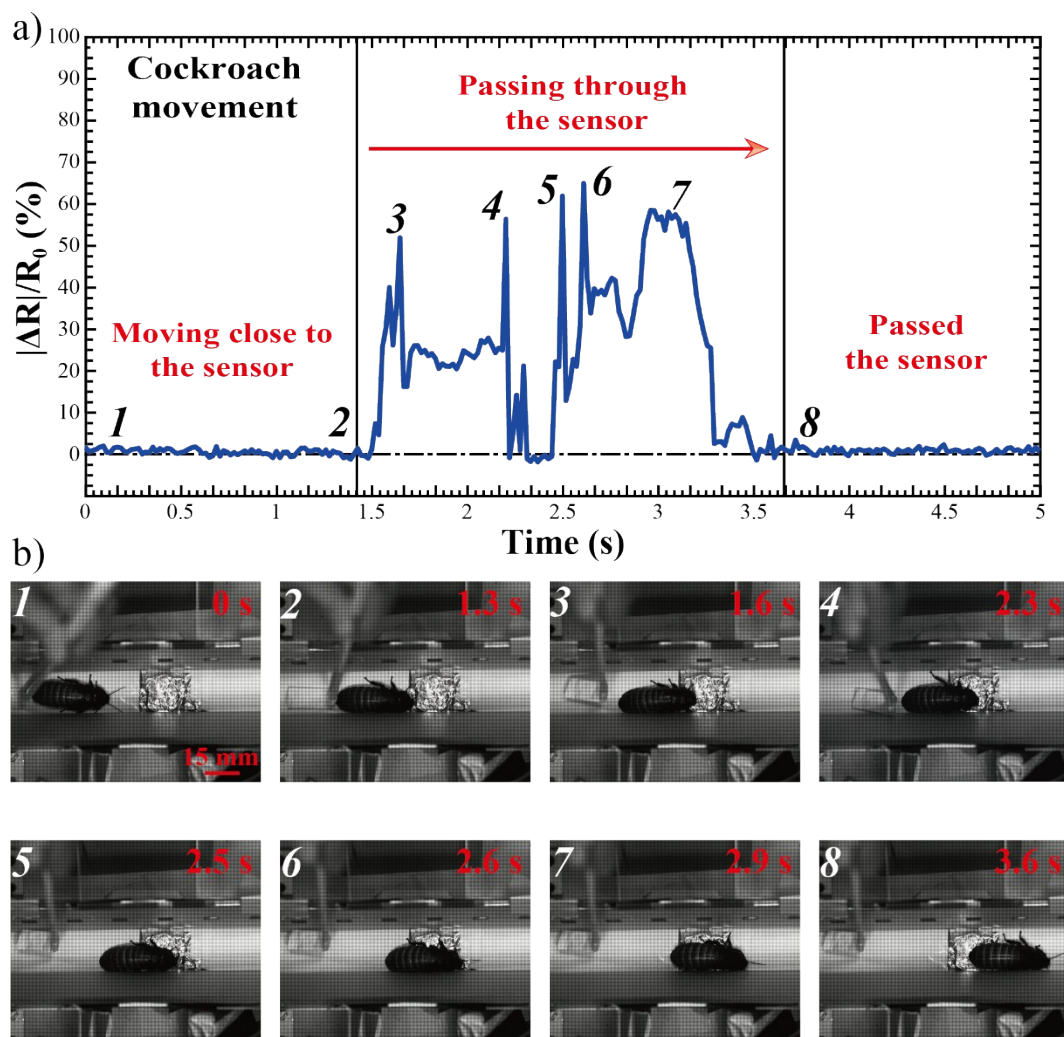
Figure S8. a) The real-time fractional resistance changes with respect to cockroach walking. b) The corresponding images recorded by a high-speed camera for the data points in a).

8. Piezoresistive response of the NPC sensor to cyclic finger tapping

To demonstrate the practicability of the NPC for sensing gentle human motion, an NPC sensor with an area of 2 cm² was used to detect finger tapping. We used a digital source meter (Keithley 2400) to detect the resistance changes and recorded the sensing process using a digital camera (EOS 70D, Canon). The real-time fractional resistance response is plotted in Fig. S9, while the insets show the corresponding images.
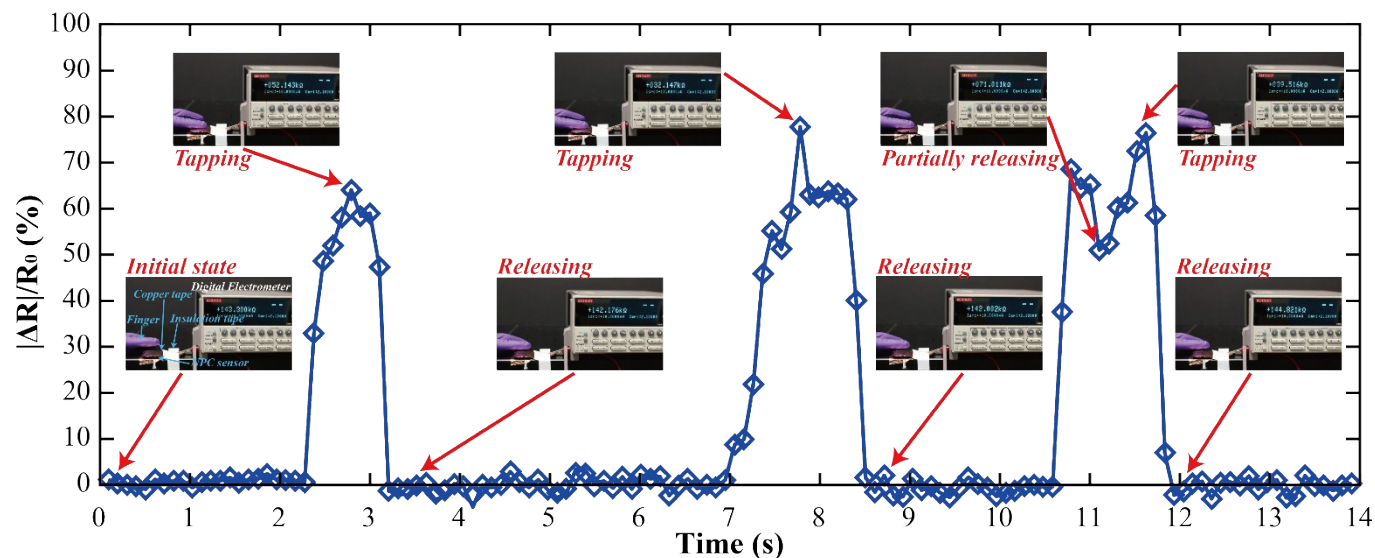

Figure S9. The fractional resistance changes with respect to cyclic finger tapping. The insets are the corresponding images.

9. Piezoresistive response of the NPC sensor to weight loading

As shown in Fig. S10, we prepared rectangular NPCs with an area of 2 cm^2 sandwiched between conductive tapes acting as electrodes, which were connected to a digital multimeter that measured the resistance. The entire pressure detection range of the NPC sensor was validated by putting weights from low to high weight (1-gram, 10-gram and 500-gram). The resistance of the NPC sensor continuously decreased with the increased loading pressure (Fig. S10), which demonstrated the NPC sensor is able to capture pressure loading up to 25 kPa. To be noted here is that due to the progressive formation of conductive pathways upon loading at different strain levels, we divided the sensitivity response of the NPC to three regimes (ultra-high sensitivity range, high sensitivity range and moderate sensitivity range). And, Fig. S10 shows the resistive responses of the NPC sensor to varying pressure loadings (50 Pa, 500 Pa and 25 kPa) in these three regimes, respectively.
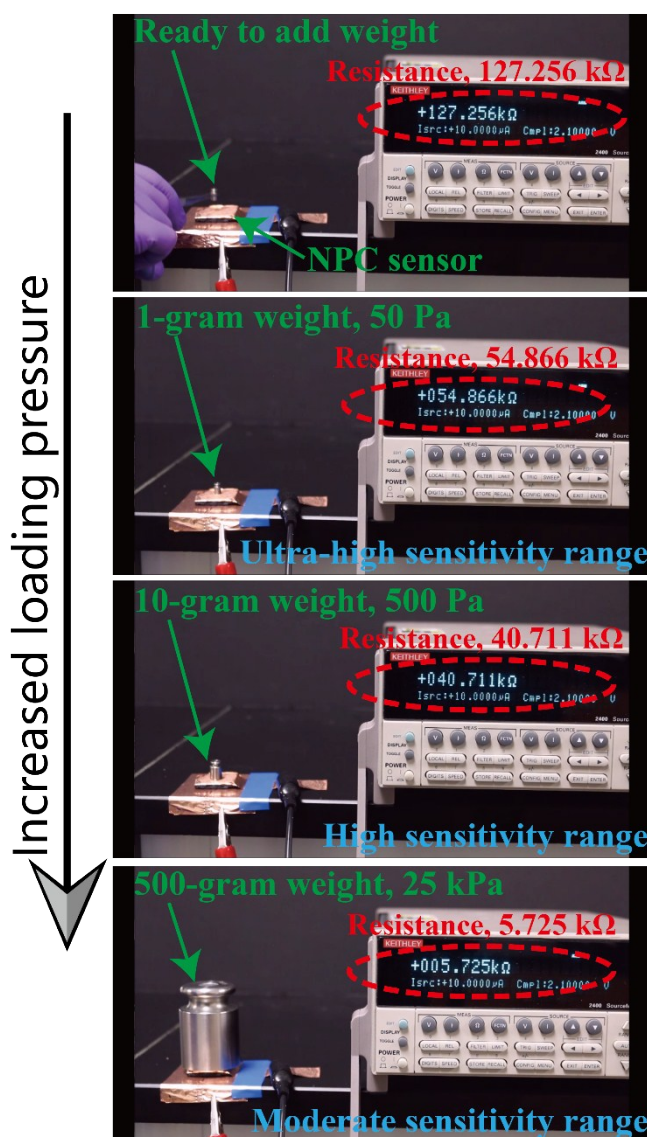
Figure S10. The resistance changes with the increasing loading pressure.

References

1   T. Yang, D. Xie, Z. Li, H. Zhu, *Mat. Sci. Eng. R* **2017**, 115, 1.
2   H. B. Yao, J. Ge, C. F. Wang, X. Wang, W. Hu, Z. J. Zheng, Y. Ni, S. H. Yu, *Adv. Mater.* **2013**, 25, 6692.
3   V. Maheshwari, R. Saraf, *Angew. Chem. Int. Edit.* **2008**, 47, 7808.
4   A. B. Joshi, A. E. Kalange, D. Bodas, S. A. Gangal, *Mater. Sci. Eng., B* **2010**, 168, 250.
5   T. Q. Trung, N. T. Tien, Y. G. Seol, N.-E. Lee, *Org. Electron*. **2012**, 13, 533.
6   L. Persano, C. Dagdeviren, Y. Su, Y. Zhang, S. Girardo, D. Pisignano, Y. Huang, J. A. Rogers, *Nat. Commun.* **2013**, 4, 1633.
7   T. Sharma, S.-S. Je, B. Gill, J. X. J. Zhang, *Sens. Actuators, A* **2012**, 177, 87.
8   C. Li, P.-M. Wu, L. A. Shutter, R. K. Narayan, *Appl. Phys. Lett*. **2010**, 96, 053502.
9   W. Wu, X. Wen, Z. L. Wang, *Science* **2013**, 340, 952.
10   G. Buchberger, R. Schwödiauer, S. Bauer, *Appl. Phys. Lett*. **2008**, 92, 123511.
11   I. Graz, M. Krause, S. Bauer-Gogonea, S. Bauer, S. P. Lacour, B. Ploss, M. Zirkl, B. Stadlober, S. Wagner, *J. Appl. Phys.*, **2009**, 106, 034503.
12   M. Ramuz, B. C. Tee, J. B. Tok, Z. Bao, *Adv. Mater.* **2012**, 24, 3223.
13   B. S. Kang, J. Kim, S. Jang, F. Ren, J. W. Johnson, R. J. Therrien, P. Rajagopal, J. C. Roberts, E. L. Piner, K. J. Linthicum, S. N. G. Chu, K. Baik, B. P. Gila, C. R. Abernathy, S. J. Pearton, *Appl. Phys. Lett.* **2005**, 86, 253502.
14   L. Viry, A. Levi, M. Totaro, A. Mondini, V. Mattoli, B. Mazzolai, L. Beccai, *Adv. Mate.* **2014**, 26, 2659.
15   J. Kim, T. Nga Ng, W. Soo Kim, *Appl. Phys. Lett.* **2012**, 101, 103308.
16   S. C. B. Mannsfeld, B. C.-K. Tee, R. M. Stoltenberg, C. V. H.-H. Chen, S. Barman, B. V. O. Muir, A. N. Sokolov, C. Reese, Z. Bao, *Nat. Mater.* **2010**, 9, 859.
17   G. Schwartz, B. C. Tee, J. Mei, A. L. Appleton, H. Kim do, H. Wang, Z. Bao, *Nat. Commun.* **2013**, 4, 1859.
18   D. J. Lipomi, M. Vosgueritchian, B. C.-K. Tee, S. L. Hellstrom, J. A. Lee, C. Fox, Z. Bao, *Nat. Nanotechnol*. **2011**, 6, 788.
19   X. Wang, Y. Gu, Z. Xiong, Z. Cui, T. Zhang, *Adv. Mater*. **2014**, 26, 1336.
20   S. Chun, Y. Kim, H. S. Oh, G. Bae, W. Park, *Nanoscale* **2015**, 7, 11652.
21   H. B. Yao, J. Ge, C. F. Wang, X. Wang, W. Hu, Z. J. Zheng, Y. Ni, S. H. Yu, *Adv. Mater*. **2013**, 25, 6692.
22   N. Lu, C. Lu, S. Yang, J. Rogers, *Adv. Funct. Mater*. **2012**, 22, 4044.
23   J. Lu, M. Lu, A. Bermak, S. Member, Y. -K. Lee, *IEEE Conf. Nanotechnology* **2007**, 1240.
24   J.-W. Han, B. Kim, J. Li, M. Meyyappan, *Appl. Phys. Lett.* **2013**, 102, 051903.
25   H. Zhang, N. Liu, Y. Shi, W. Liu, Y. Yue, S. Wang, Y. Ma, L. Wen, L. Li, F. Long, Z. Zou, Y. Gao, *ACS Appl. Mater. Interfaces* **2016**, 8, 22374.
26   Q. Fan, Z. Qin, S. Gao, Y. Wu, J. Pionteck, E. Mäder, M. Zhu, *Carbon* **2012**, 50, 4085.
27   27I. Kang, M. J. Schulz, J. H. Kim, V. Shanov, D. Shi, *Smart Mater. Struct.* **2006**, 15, 737
28   Y. R. Jeong, H. Park, S. W. Jin, S. Y. Hong, S. S. Lee J. S. Ha, *Adv. Funct. Mater.* **2015**, 25, 4228.
29   V. Eswaraiah, K. Balasubramaniam, S. Ramaprabhu, *Nanoscale* **2012**, 4 1258.
30   C. S. Boland, U. Khan, G. Ryan, S. Barwich, R. Charifou, A. Harvey, C. Backes, Z. Li, M. S. Ferreira, M. E. Möbius, R. J. Young, J. N. Coleman, R. J. Young, *Science* **2016,** 354, 1257.
31   W. Li, J. Guo, D. Fan, *Adv. Mater. Technol.* **2017**, 1700070.
32   C. Pang, G.-Y. Lee, T.-I. Kim, S. M. Kim, H. N. Kim, S.-H. Ahn, K.-Y. Suh, *Nat. Mater.* **2012**, 11, 795.
33   M. Amjadi, A. Pichitpajongkit, S. Lee, S. Ryu, I. Park, *ACS Nano* **2014**, 8, 5154.